ORIGINAL ARTICLE

lajss.org© Latin American Journal of Solids and Structures

www.lajss.org

Optimizing the Formation of Hollow Annular Shaped Charges Through a Novel Charge Compensation Method: External Experiment Validation, Simulation, and Predictive Model

Liudong Zheng[a], Xin Jia[a,*], Zhengxiang Huang[a], Yuze Chen[a]

[a] School of Mechanical Engineering, Nanjing University of Science and Technology, Nanjing 210094, China. Email: 1255454393@qq.com, jiaxin@mail.njust.edu.cn, huangyu@mail.njust.edu.cn, 2415843833@qq.com

* Corresponding Author

https://doi.org/10.1590/1679-7825/e8877

Abstract

The design optimization of Annular Shaped Charge (ASC) is highly complex and nonlinear. Traditional ASC optimization focuses on liner structure using empirical methods, while optimization for annular charges is scarce because slight charge variations significantly alter the annular penetrator morphology. To address this, we propose a predictive model for Optimal Charge Compensation Amount (OCCA) of Hollow Annular Shaped Charge (HASC) by integrating Finite Element Method with Multilayer Perceptron (FEM-MLP). Through dimensional analysis and theoretical calculations, we identified four input parameters. Using these, 1431 data points were generated to train and test the MLP. Compared with SVR, Random Forest, and Linear Regression using 5-fold cross-validation, the MLP showed superior prediction accuracy and generalization. The trained MLP predicted OCCA for random and experimental structures, and numerical simulations confirmed high accuracy and generalization. The charge compensation method is broadly applicable for similar HASC structures. The optimized annular jet exhibits no deviation and delayed fracture, providing insights for annular jet penetration into targets.

Keywords

Hollow annular shaped charge; Numerical simulation; Multilayer perceptron; Charge compensation method

Graphical abstract

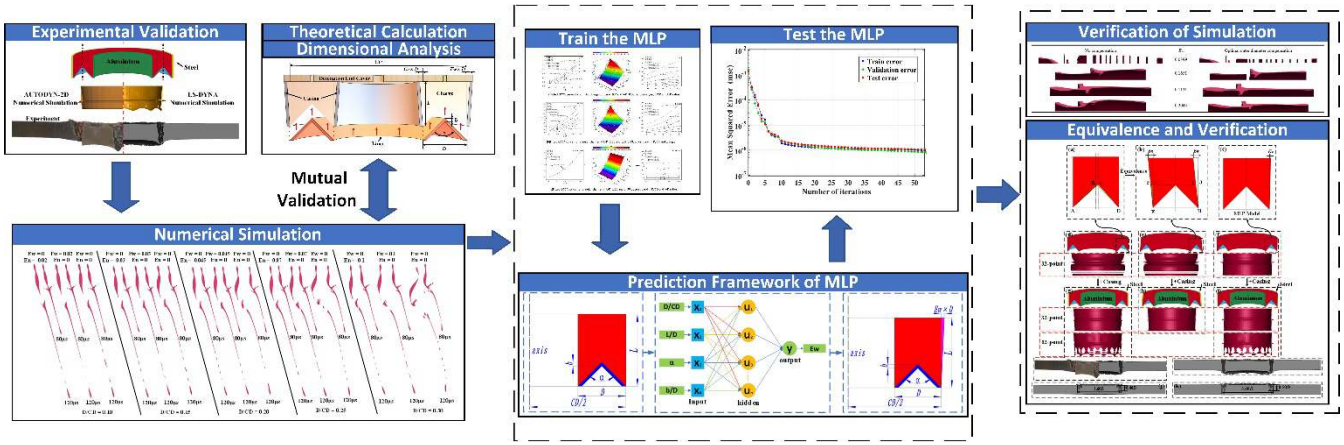

Received October 23, 2025. In revised form April 08, 2026. Accepted April 10, 2026. Available online April 22, 2026.
https://doi.org/10.1590/1679-7825/e8877

Latin American Journal of Solids and Structures. ISSN 1679-7825. Copyright © 2026. This is an Open Access article distributed under the terms of the Creative Commons Attribution License, which permits unrestricted use, distribution, and reproduction in any medium, provided the original work is properly cited.

Introduction

Shaped charge technology can effectively damage hard targets (Hu F. et al. 2017, Liu J. et al. 2018, Wu J. et al. 2007) and has been widely applied in various fields (Jia X. et al. 2013, Xu W. et al. 2019, Xiao Q Q. et al. 2017), including petroleum exploration (Lee W H. et al. 2002, Elshenawy T. et al. 2013), fortification (Niu Y. et al. 2024, Zhu Q. et al, 2018), anti-tank operations (Jia X. et al. 2015, Micković D. et al. 2016), and underwater explosions (Zhang Z. et al. 2017, Cao C. et al. 2025). However, with the development of multi-layered protective armor and grid armor, the damage effectiveness of traditional shaped-charge warheads against multi-layered protective targets has been significantly restricted. To address this, some scholars have proposed using tandem warheads for damaging multi-layered protective targets. Yet, for tandem warheads aiming to achieve large-diameter openings in targets, the conventional precursor shaped-charge warhead fails to meet the requirements, whereas the adoption of an Annular Shaped Charge (ASC) can achieve a large-diameter penetration effect. Leidel (1978) designed a novel charge configuration by adding a steel cylinder to the charge, forming an annular charge structure, and conducted preliminary explorations into annular jets.

Currently, existing ASC primarily fall into two categories: solid annular and hollow annular shaped charge. For solid ASC, Wang et al. (2009) designed a feasible W-shaped shaped charge based on the principle of equal impulse for both inner and outer liners, and conducted simulation analyses. Xu et al. (2019)(2019) proposed a hole-centered annular shaped charge (HASC), validated it experimentally, and investigated the penetration performance of annular jets formed by different liner materials. Zhang et al. (2022) enhanced underwater penetration using a novel annular charge. For HASC, Liu et al. (2013)(2023) studied multi-point initiation of annular charges via LS-DYNA and conducted experimental validation. Li et al. (2025) optimized HASC with an eccentric conical liner and performed static armor-penetration tests. For composite ASC, Hu et al. (2021) designed a novel composite annular charge configuration for damaging underwater structures, with mutual validation through numerical simulations and experiments. Ren et al. (2021) devised a warhead combining an annular jet and a centrally located Explosively Formed Projectile, with experimental results demonstrating that this composite warhead could create holes in concrete walls with diameters exceeding 2.5 times the charge diameter.

ASC differs from Shaped Charge (SC) in that, when assuming a constant liner cross sectional caliber D for ASC, the morphology of the annular penetrator undergoes significant alterations with variations in the charge diameter CD. This constitutes a crucial factor influencing the design and optimization of ASC. Current research on ASC predominantly treats this factor as either a fixed value or one among a multitude of variable factors (such as charge height L, liner wall thickness b, etc.) in comparative studies utilizing the control variable method. Optimization efforts for ASC are mostly conducted by refining the annular liner structure under a single D/CD condition(Huang QT. 2008), including methods like offsetting or compensating the liner wall thickness(Hou J. 2023, Chen J. 2023), or adopting an asymmetric liner configuration to achieve similar objectives (LI Zhaoting. et al. 2025). Gao(2024) employed simulation software to model the formation process of ASC under varying rotation diameters.

Machine learning has been widely researched and applied in fields such as biology (Ponnarengan H. et al. 2024), pharmaceuticals(Rahman SIU. et al. 2025), and mechanical/engineering technologies (Koide R M. et al. 2015, Mahmoodi M. et al. 2016).Given that the optimization of shaped charge penetrators involves a complex, multi-parameter-coupled nonlinear problem, some scholars have proposed employing machine learning (ML) techniques to address this issue(Cao C. et al. 2025, Wu B. et al. 2022, Zhao Z. et al. 2024). On HASC, Chen et al. (2022) integrated numerical simulation results with a Back Propagation neural network and employed a genetic algorithm to optimize a conical-ring liner, ultimately identifying the optimal conical-ring liner structure. Xu. et al. (2021) proposed utilizing a Convolutional Neural Network for the design optimization of solid ASC.

In general, the formation and penetration capability of annular jets are closely tied to the charge configuration and liner structure. Currently, research on ASC both domestically and internationally primarily focuses on optimizing the liner structure under a single charge configuration. However, the manufacturing process of liners cannot guarantee consistency, and once the ratio of the liner cross-sectional caliber D to the charge diameter CD is altered, the optimized structural data becomes inapplicable to the new configuration. To address this issue, this paper proposes a systematic design method for HASC. It establishes a theoretical calculation model for annular charge compensation method and an MLP prediction model for HASC-OCCA, conducting 5-fold cross-validation and comparing the model with SVR, Random Forest, and Linear Regression. The experimental model from reference (LI Zhaoting. et al. 2025) is equivalently represented and utilized to validate the reliability of this study, revealing the patterns of annular jet modification through charge compensation method.

Figure 1 illustrates the MLP design framework for HASC-OCCA in this paper.

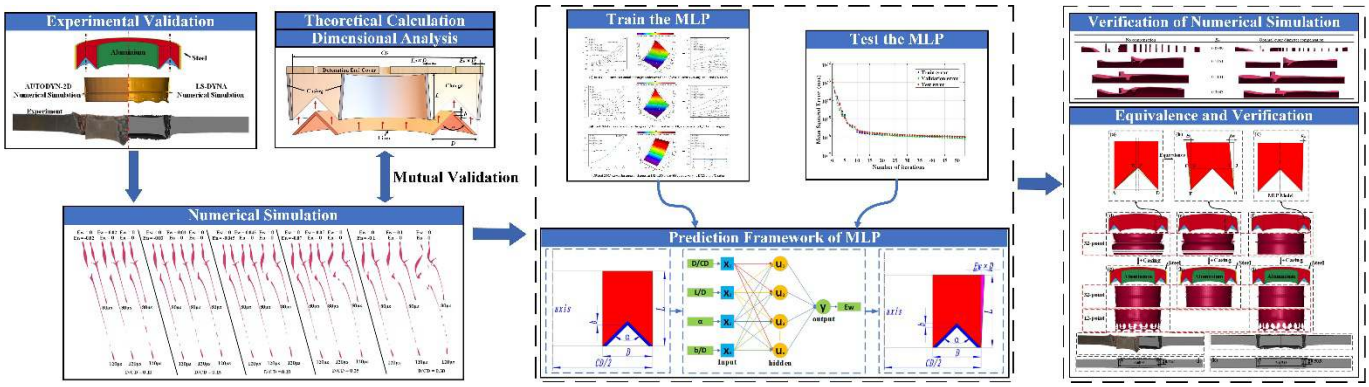

Figure 1. MLP design framework for HASC-OCCA

Dimensional Analysis and Theoretical Model Formulation for HASC Utilizing Charge Compensation Method

Dimensional Analysis of the Forming Process for HASC

During the forming process of hollow annular shaped charges, ensuring the non-deviation of the formed charge is directly related to the radial collapse velocity of the annular liner's infinitesimal elements and indirectly related to their axial collapse velocity. The factors influencing these radial and axial collapse velocities primarily revolve around the relevant dimensional and material physical quantities of the liner's infinitesimal elements, the corresponding charge's dimensional and material physical quantities, and the relevant dimensional and material physical quantities of the external casing corresponding to these elements. The following sections will provide a detailed analysis of these physical quantities. The structural diagram of HASC is shown in Figure 2.

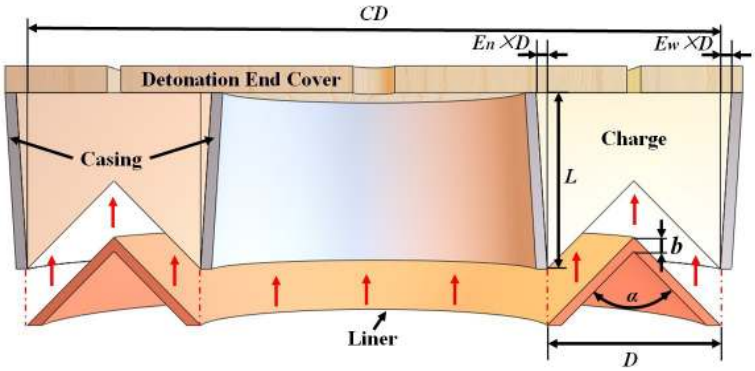

Figure 2. Structural diagram of HASC

(1)Liner

There are numerous independent physical quantities describing the infinitesimal elements of the annular liner. As illustrated in the figure, the independent dimensional physical quantities include: the cross sectional caliber of the annular liner, denoted as D , the diameter of the liner, denoted as CD , the cone angle of the liner, denoted as α , and the thickness at the apex of the liner, denoted as b . The independent material physical quantities are: the density of the liner material, denoted as ρ_i , the strength of the liner material, denoted as σ_i , the sound speed in the liner material, denoted as C_i , and the elastic modulus of the liner material, denoted as E_i.

(2)Charge

The charge corresponding to the liner infinitesimal elements is divided into axial charge and radial charge. For the axial charge, the independent dimensional physical quantities include: the height of the charge, denoted as L. For the radial charge, the independent dimensional physical quantities are: the outer diameter charge compensation amount, denoted as E_w (which can be negative, dimensionless parameter), and the inner diameter charge compensation amount, denoted as E_n (which can be negative, dimensionless parameter). The independent material physical quantities of the charge are: the initial density of the charge, denoted as ρ_0 , the detonation velocity of the explosive, denoted as D_e , and the polytropic index of the detonation gas, denoted as γ.

(3)Casing

According to the research conducted by numerous scholars, the casing also exerts a significant influence on the forming process of the HASC. The independent dimensional physical quantities of the casing include: the outer diameter casing thickness, denoted as k_w (dimensionless parameter), and the inner diameter casing thickness, denoted as k_n (dimensionless parameter). The independent material physical quantities of the casing are: the casing density, denoted as ρ_k , the material strength of the casing, denoted as σ_k , the sound speed in the casing material, denoted as C_k , and the elastic modulus of the casing material, denoted as E_k.

(4)Initiation of the Charge

The independent physical quantities related to charge initiation are: initiation radius r_i , and the time t after initiation.

After determining that the shape of the annular liner is a conical shape with a uniform wall - thickness, the general functional relationship for the collapse velocity of the infinitesimal element of the annular liner can be expressed as

$$V_i = f\left(D, CD, \alpha, b, \rho_i, \sigma_i, C_i, E_i, E_w, E_n, L, \rho_0, D_e, \gamma, K_w, K_n, \rho_k, \sigma_k, C_k, E_k, r_0, t\right) \tag{1}$$

Under the condition that the relevant material parameters of the shaped charge liner, explosive, and casing remain unchanged in the above equation, the general functional relationship for the collapse velocity of the infinitesimal element of the annular liner transforms into

$$V_i = f\left(D, CD, \alpha, b, E_w, E_n, K_w, K_n, L, t\right) \tag{2}$$

The equation is subjected to non-dimensionalization. By selecting the independent dimensional physical quantities as D,t , it is reformulated in a non-dimensional form.

$$\frac{V_i}{Dt} = f\left(\frac{CD}{D}, \alpha, \frac{b}{D}, E_w, E_n, K_w, K_n, \frac{L}{D}\right) \tag{3}$$

Since f () merely denotes the existence of a certain functional relationship rather than corresponding to a specific functional expression, the above equation can also be rewritten as

$$V_i = Dt \cdot f\left(\frac{D}{CD}, \alpha, \frac{b}{D}, E_w, E_n, K_w, K_n, \frac{L}{D}\right) \tag{4}$$

Theoretical Model of HASC Optimized by Charge Compensation Method and Analysis of Collapse Velocity

The HASC exhibits axial symmetry. Now, we select a cross section of the HASC for analysis and establish a coordinate system. The Y-axis is set up vertically downward along the axis of symmetry of the annular charge, and the X-axis is set up horizontally to the right along the bottom end of the annular charge, as shown in Figure 3. The initiation method is approximately equivalent to the central point initiation of a traditional shaped charge. The top of the liner is the first point to be reached by the shock wave after the explosive is initiated. The explosive above the top of the liner drives the axial motion of the liner, while the explosive on both sides of the liner drives its radial motion. Let D_e represent the propagation velocity of the detonation wave. The dashed line is the tangent to the outer contour of the liner at the infinitesimal element A, and the angle between this tangent and the wave velocity is ϑ. The angle between the collapse velocity V_A and the normal at point A is δ. Then, the velocity of the detonation wave passing through the surface of the liner is:

$$U = \frac{D_e}{\cos\theta} \tag{5}$$

The formula for the projection angle is:

$$\delta = \arcsin\frac{V_A}{2U} \tag{6}$$

When the collapse velocity V_A is resolved into components along the charge axis direction and perpendicular to the charge axis direction, it can be expressed as:

$$\vec{V}_A = V_{AX}\vec{i} + V_{AY}\vec{j} \tag{7}$$

V_{AY} is the component that drives the infinitesimal element on the annular shaped charge liner to move along the charge axis direction, and its primary function is to elongate the annular shaped charge jet.

V_{AX} is the component that causes the liner infinitesimal element to move in a direction perpendicular to the charge axis. The radial velocity plays a crucial role in the formation of a stable annular shaped charge jet.

The parameters of the annular shaped charge liner are shown in Figure 3.

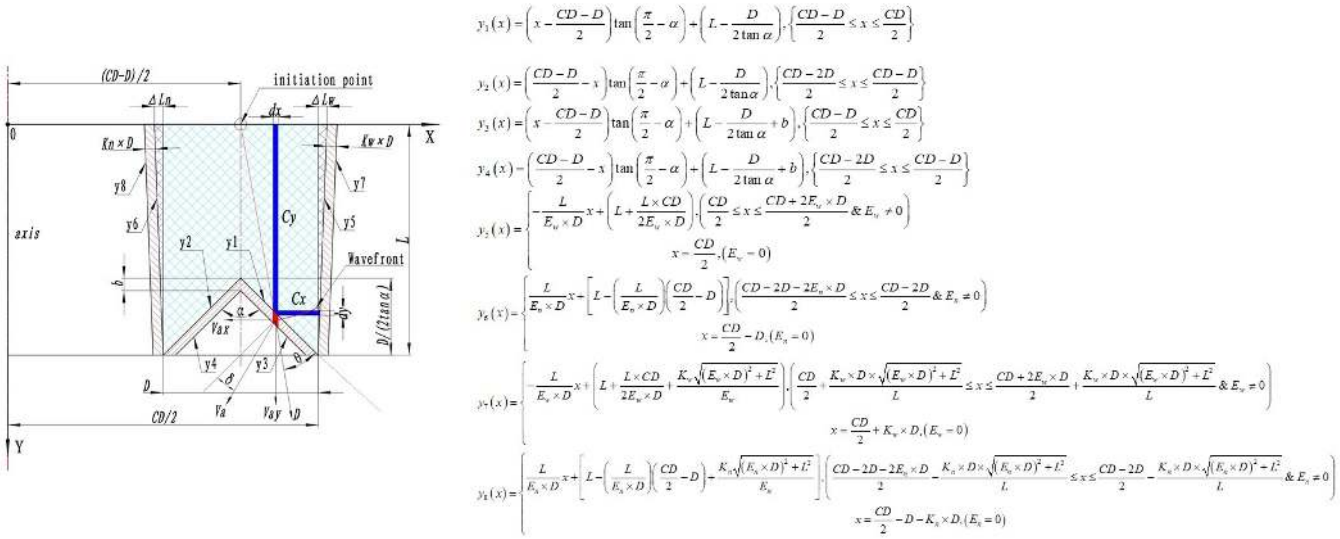

$$y_1(x)=\left(x-\frac{CD-D}{2}\right)\tan\left(\frac{\pi}{2}-\alpha\right)+\left(L-\frac{D}{2\tan\alpha}\right),\left\{\frac{CD-D}{2}\le x\le\frac{CD}{2}\right\}$$

$$y_2(x)=\left(\frac{CD-D}{2}-x\right)\tan\left(\frac{\pi}{2}-\alpha\right)+\left(L-\frac{D}{2\tan\alpha}\right),\left\{\frac{CD-2D}{2}\le x\le\frac{CD-D}{2}\right\}$$

$$y_3(x)=\left(x-\frac{CD-D}{2}\right)\tan\left(\frac{\pi}{2}-\alpha\right)+\left(L-\frac{D}{2\tan\alpha}+b\right),\left\{\frac{CD-D}{2}\le x\le\frac{CD}{2}\right\}$$

$$y_4(x)=\left(\frac{CD-D}{2}-x\right)\tan\left(\frac{\pi}{2}-\alpha\right)+\left(L-\frac{D}{2\tan\alpha}+b\right),\left\{\frac{CD-2D}{2}\le x\le\frac{CD-D}{2}\right\}$$

$$y_5(x)=\begin{cases}-\dfrac{L}{E_w\times D}x+\left(L+\dfrac{L\times CD}{2E_w\times D}\right),\left(\dfrac{CD}{2}\le x\le\dfrac{CD+2E_w\times D}{2}\ \&\ E_w\neq 0\right)\\ x=\dfrac{CD}{2},(E_w=0)\end{cases}$$

$$y_6(x)=\begin{cases}\dfrac{L}{E_n\times D}x+\left[L-\left(\dfrac{L}{E_n\times D}\right)\left(\dfrac{CD}{2}-D\right)\right],\left(\dfrac{CD-2D-2E_n\times D}{2}\le x\le\dfrac{CD-2D}{2}\ \&\ E_n\neq 0\right)\\ x=\dfrac{CD}{2}-D,(E_n=0)\end{cases}$$

$$y_7(x)=\begin{cases}-\dfrac{L}{E_w\times D}x+\left(L+\dfrac{L\times CD}{2E_w\times D}+\dfrac{K_w\sqrt{(E_w\times D)^2+L^2}}{E_w}\right),\left(\dfrac{CD}{2}+\dfrac{K_w\times D\times\sqrt{(E_w\times D)^2+L^2}}{L}\le x\le\dfrac{CD+2E_w\times D}{2}+\dfrac{K_w\times D\times\sqrt{(E_w\times D)^2+L^2}}{L}\ \&\ E_w\neq 0\right)\\ x=\dfrac{CD}{2}+K_w\times D,(E_w=0)\end{cases}$$

$$y_8(x)=\begin{cases}\dfrac{L}{E_n\times D}x+\left[L-\left(\dfrac{L}{E_n\times D}\right)\left(\dfrac{CD}{2}-D\right)-\dfrac{K_n\sqrt{(E_n\times D)^2+L^2}}{E_n}\right],\left(\dfrac{CD-2D-2E_n\times D}{2}-\dfrac{K_n\times D\times\sqrt{(E_n\times D)^2+L^2}}{L}\le x\le\dfrac{CD-2D}{2}-\dfrac{K_n\times D\times\sqrt{(E_n\times D)^2+L^2}}{L}\ \&\ E_n\neq 0\right)\\ x=\dfrac{CD}{2}-D-K_n\times D,(E_n=0)\end{cases}$$

Figure 3. Theoretical model of HASC optimized based on the charge compensation method

Basic assumptions for the infinitesimal elements of the liner: (1) Instantaneous detonation of the explosive upon initiation; (2) The infinitesimal elements of the liner do not interact with each other.

Calculation of the Collapse Velocity of the Outer/ (Inner) Ring Infinitesimal Elements of the Annular Shaped Charge Liner

When located at point *i* on the outer/(inner) ring of the annular shaped-charge liner, the mass M_i of the liner infinitesimal element and the mass M_{yi} of the longitudinal explosive C_{yi} at point *i* can be expressed as:

$$M_i = \rho_i \times 2\pi\int_{t_i}^{t_{i+1}} x\left[y_{3/4}(x)-y_{1/2}(x)\right]dx \tag{8}$$

$$M_{yi} = \rho_0 \times 2\pi\int_{t_i}^{t_{i+1}} xy_{1/2}(x)dx \tag{9}$$

$$M_{xi} = \rho_0 \times \pi\int_{u_i}^{u_{i+1}} \left\{\left(y_{5/6}^{-1}(x)\right)^2-\left[y_{1/2}^{-1}(x)\right]^2\right\}dy \tag{10}$$

$$M_{ki} = \rho_k \times \pi\int_{u_i}^{u_{i+1}} \left\{\left(y_{7/8}^{-1}(x)\right)^2-\left[y_{5/6}^{-1}(x)\right]^2\right\}dy \tag{11}$$

In the formula , ρ_i is the density of the annular shaped charge liner,, ρ_0 is the density of the explosive , ρ_k is the density of the casing , $y_{3/4}(x)$ is the equation for the outer/(inner) ring profile of the liner on the side away from the charge, and $y_{1/2}(x)$ is the equation for the outer/(inner) ring profile of the liner on the side adjacent to the charge.

The mass ratio of the liner infinitesimal element at point *i* to the longitudinal explosive is expressed as:

$$\mu_{1i}=\frac{M_i}{M_{yi}}=\frac{\rho_i\int_{t_i}^{t_{i+1}}x\left[y_{3/4}(x)-y_{1/2}(x)\right]dx}{\rho_0\int_{t_i}^{t_{i+1}}xy_{1/2}(x)dx} \tag{12}$$

Through substitution, the axial velocity V_{yi} is determined. As can be inferred from the equation, the magnitude of V_{yi} is exclusively a function of μ_{1i} , with V_{yi} decreasing as μ_{1i} increases.

$$V_{yi}=\sqrt{2E}\left\{\frac{1}{3}\left[\left(2\mu_{1i}\right)^2+5\mu_{1i}+1\right]\right\}^{-\frac{1}{2}} \tag{13}$$

In the formula , $\sqrt{2E}$ represents the Gurney constant of the explosive;

Subsequently, the radial velocity V_{xi} is examined. Utilizing the formula for explosive-driven cylindrical motion (Chanteret P Y. 1983), a hypothetical fixed rigid wall is introduced to eliminate the explosive impulse term in the energy conservation equation, thereby yielding the equation for the rigid wall radius R_x as presented below:

$$\begin{aligned}&R_x^3+3R_x\left[\left(R_1+R_2\right)\times\frac{\rho_0}{\rho_{cj}}\times\left(\frac{M_1}{M_x}R_2+\frac{M_2}{M_x}R_1\right)+R_1R_2\right]\\&-3\left(R_1+R_2\right)R_1R_2\left(\frac{2}{3}+\frac{\rho_0}{\rho_{cj}}\times\left(\frac{M_1}{M_x}+\frac{M_2}{M_x}\right)\right)=0\end{aligned} \tag{14}$$

The schematic diagram is depicted in Figure 4.

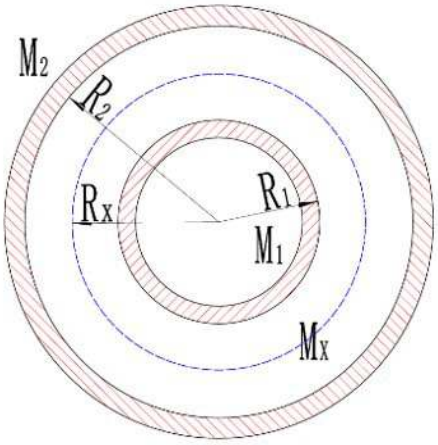

Figure 4. Schematic diagram of cylindrical motion driven by a hollow annular charge

the formula for calculating the velocity V_1 of the inner wall of the cylinder is as follows:

$$V_1=\sqrt{2E}\left[\left(\frac{R_2^2-R_1^2}{R_x^2-R_1^2}\right)\frac{M_1}{M_x}+\frac{1}{6}\right]^{-\frac{1}{2}} \tag{15}$$

The formula for calculating the velocity V_2 of the outer wall of the cylinder is as follows:

$$V_2 = \sqrt{2E}\left[\left(\frac{R_2^2 - R_1^2}{R_w^2 - R_x^2}\right)\frac{M_2}{M_x} + \frac{1}{6}\right]^{-\frac{1}{2}} \tag{16}$$

For the outer ring of the annular shaped charge, the annular liner serves as the inner wall of the cylinder, while the outer - diameter shell of the annulus acts as the outer wall of the cylinder. Conversely, for the inner ring, the annular liner functions as the outer wall of the cylinder, and the inner - diameter shell serves as the inner wall of the cylinder. This distinction should be duly noted during calculations.

According to Equation (14) or Equation (15), the radial collapse velocity of the liner element is calculated; according to Equation (13), the axial collapse velocity of the liner element is calculated; and according to Equation (7), the resultant collapse velocity of the liner element is obtained.

Numerical simulation and theoretical validation yielded the OCCA

Verification of Model Reliability

To validate the reliability of the material parameters and mesh model used in numerical simulations, a three-dimensional LS-DYNA model of the annular shaped charge from Reference (LI Zhaoting. et al. 2025) was established. This model was compared with the numerical simulation results obtained using AUTODYN-2D in the same reference. Numerical simulations were conducted using a model with identical material parameters as those in the reference. The formation morphology of the annular jet was compared with the numerical simulation results in the reference, and the penetrated target plate was compared with the experimental results presented in the reference. The conventional annular jet formation and penetration results for a non-eccentric liner are depicted in Figure 5. During the formation process, the head of the annular jet continuously deviates inward, ultimately creating an inwardly inclined crater upon penetration. Meanwhile, the slug deviates outward, enlarging the aperture based on the original penetration crater, and ultimately, the annular jet fails to penetrate the 0.8D armor steel target. By eccentrically positioning the top of the annular liner outward, the resulting annular jet, as shown in Figure 6, penetrates the target plate with a thickness of 0.8D. The penetration morphology of the experimental target plate reveals whether the annular jet has deviated. LS-DYNA can simulate the formation morphology of the annular jet initiated at 12 points in the experiment. The insufficient number of initiation points leads to a wavy head of the annular jet, an effect that cannot be replicated using AUTODYN-2D.

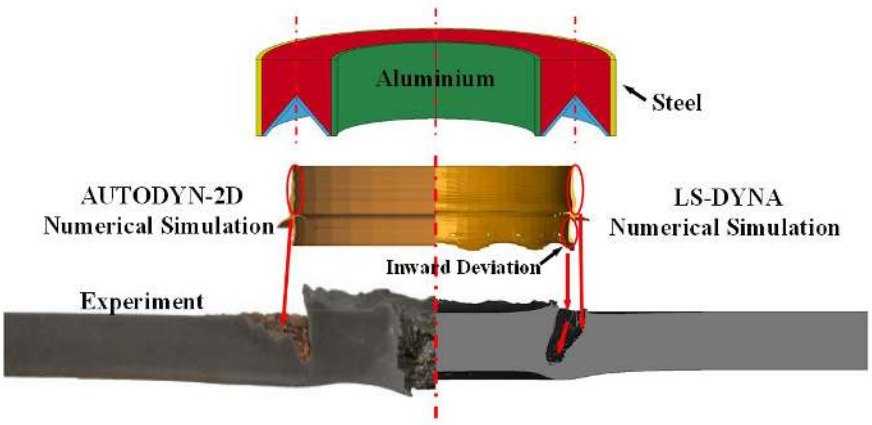

Figure 5. Formation and penetration results of the annular jet with a non-eccentric liner

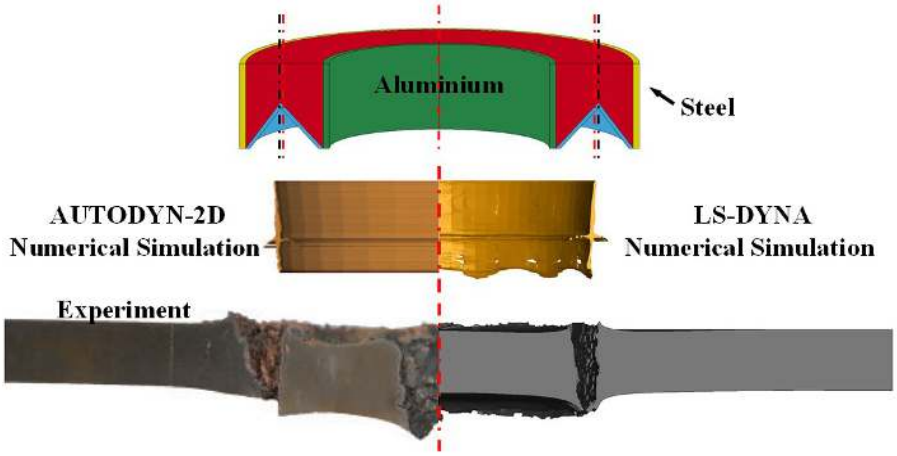

Figure 6. Formation and penetration results of the annular jet with an outwardly eccentric liner

Material Parameters for Numerical Simulation

In this study, LS-DYNA was employed to conduct numerical simulations on the formation of HASC. The research focuses separately on optimizing the formation of HASC using the charge compensation method. Given the axisymmetric structure of HASC, a quarter simulation model was established, as illustrated in Figure 7, encompassing three Eulerian mesh sections: the explosive, the liner, and the air.

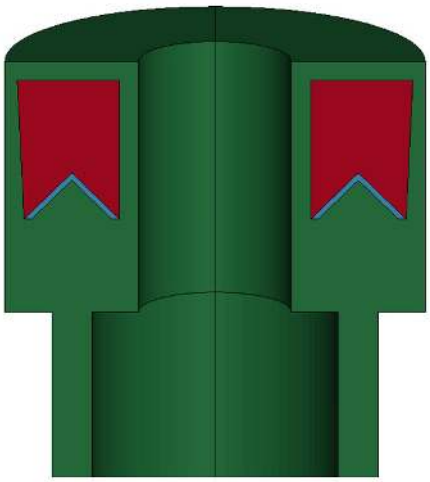

Figure 7. Simulation computational model

The explosive material selected is Octol, utilizing the HIGH_EXPLOSIVE_BURN constitutive equation and the JWL equation of state. The pressure of the detonation products satisfies the following equation:

$$P = A\left(1-\frac{\omega\eta}{R_1}\right)e^{-R_1/\eta}+B\left(1-\frac{\omega\eta}{R_2}\right)e^{-R/\eta}+\omega\eta\rho_0 e_0 \tag{17}$$

The material parameters of the explosive and the parameters of its equation of state are presented in Table 1.

Table 1. Material parameters and equation of state parameters for Octol explosive

ρ_0/(g/cm^3)	D_J/(m/s)	P_{CJ}/GPa	A/GPa	B/GPa	R_1	R_2	ω	e_0/(kJ/m^3)
1.821	8480	34.2	748.6	13.38	4.5	1.2	0.38	9.6E+6

Copper is selected as the liner material. The JOHNSON-COOK material model and the GRUNEISEN equation of state are employed. The functional expression of the JOHNSON-COOK material model is as follows::

$$\sigma_y = \left(A + B\overline{\varepsilon}^{p^n}\right)\left(1 + C\ln\dot{\varepsilon}^*\right)\left(1 - T^*\right) \tag{18}$$

In the formula , A , B , C , n and m are all material parameters ; $\overline{\varepsilon}^p$ represents the equivalent plastic strain; $\dot{\varepsilon}^* = \dot{\overline{\varepsilon}}^p / \dot{\varepsilon}_0$ with $\dot{\varepsilon}_0$ =1s^{-1} is normalized effective plastic strain rate, and T^* is the homologous temperature。

$$T^* = \frac{T - T_r}{T_m - T_r} \tag{19}$$

Where T_r is the room temperature and T_m is the melting temperature.

The material parameters of copper are shown in Table 2.

Table 2. The material parameters of copper

ρ_0/(g/cm^3)	E/(m/s)	G/GPa	v	A/MPa	B/MPa	T_m/K	T_r/K	n	c	m
8.93	1.38	47.7	0.35	90	292	1360	293	0.45	0.025	1.09

Copper employs the GRUNEISEN equation of state to describe the material pressure under compression conditions.

$$P = \frac{\rho_0 C_0^2 \mu\left[1 + \left(1 - \frac{\gamma_0}{2}\right)\mu - \frac{a}{2}\mu^2\right]}{\left[1 - \left(S_1 - 1\right)\mu - S_2\frac{\mu^2}{\mu+1} - S_3\frac{\mu^3}{\left(\mu+1\right)^2}\right]} + \left(\gamma_0 + a\mu\right)E \tag{20}$$

Material pressure under expansion conditions:

$$P = \rho_0 C_0^2 \mu + \left(\gamma_0 + a\mu\right)E \tag{21}$$

In the formula , $\mu = \rho/\rho_0 - 1$,ρ is the density of the material after deformation , ρ_0 is the initial density of the material , C_0 is the intercept of the shock wave velocity and particle velocity curve , S_1 , S_2 , and S_3 are the slope coefficients of the shock wave velocity and particle velocity curve , γ_0 is the GRUNEISEN constant; and a is a constant corresponding to γ_0。 The specific parameters are shown in Table 3.

Table 3. Parameters for the Equation of State of Copper

C_0/(km/s)	S_1	S_2	a	γ_0
3.94	1.49	0	0	1.99

The air is modeled using the NULL material model and the LINEAR_POLYNOMIAL equation of state , with the equation expressed as:

$$P = C_0 + C_1\mu + C_2\mu^2 + C_3\mu^3 + \left(C_4 + C_5\mu + C_6\mu^2\right)E \tag{22}$$

In the formula , C_0 , C_1 , C_2 , C_3 , C_4 , C_5 and C_6 are constants , $\mu = \rho/\rho_0 - 1$, ρ and ρ_0 represent the current density and initial density, respectively. The primary material parameters of air are listed in Table 4.

Table 4. Air material parameters

ρ/(g/cm^3)	C_4	C_5	E/(J/kg)
1.28E-3	0.4	0.4	0.25

Numerical simulation adjustment utilizing OCCA and theoretical calculation verification

The influence of variations in D/CD on OCCA

Before determining the OCCA for different HASC structures, it is essential to first ascertain the impact of variations in *D/CD* on OCCA. By setting *D* at 100 mm and altering the value of *CD*, five variables of *D/CD* were established: 0.10, 0.15, 0.20, 0.25, and 0.30. With *L/D* fixed at 1.50, *b/D* at 0.08, and α at 90°, Table 5 presents the OCCA values for different *D/CD* ratios, while Figure 8 illustrates the differences in the formation morphology of the annular jet at 80 μs and 120 μs for various *D/CD* ratios, with and without compensation (depicted through cross-sectional formation diagrams on the right side of the HASC's axis of symmetry).

Based on Table 5 and Figure 8, it can be observed that when no charge compensation amount (E_w and E_n equal to 0) is applied to the HASC, the annular jet exhibits deviation. However, upon optimizing the HASC using the charge compensation method by increasing the OCCA (with E_w and E_n not equal to 0), the HASC returns to a collimated state. Once the OCCA is determined, it is reflected in E_w and E_n satisfying the following equation:

$$OCCA=E_w-E_n \tag{23}$$

Among them, E_w and E_n the dimensionless parameters of the outer charge compensation amount and the inner charge compensation amount, respectively, defined as follows:

$$E_w=\frac{\Delta L_w}{D}, E_n=\frac{\Delta L_n}{D} \tag{24}$$

Where *D* is the cross-sectional caliber of the liner (unit: mm), ΔL_w is the outer charge compensation amount (unit: mm), and ΔL_n is the inner charge compensation amount (unit: mm). The geometric meanings of ΔL_w and ΔL_n are illustrated in Figure 3. It is worth mentioning that when ΔL_w and ΔL_n are negative, it indicates a reduction in the corresponding charge.

Since ΔL_w, ΔL_n, and *D* all have the dimension of length, both E_w and E_n are dimensionless parameters, and their difference, OCCA, is also dimensionless. The sign and magnitude of OCCA directly reflect the direction and extent of charge compensation: when OCCA is greater than 0, it indicates that the outer compensation amount exceeds the inner compensation amount; when OCCA is less than 0, the inner compensation amount is greater; when OCCA equals 0, the inner and outer compensation amounts are equal (no compensation or balanced compensation). By optimizing the value of OCCA, the originally deflected annular jet can be restored to a collimated state, thereby improving the convergence performance of the shaped jet.

Table 5. OCCA for Different D/CD Ratios

D/CD=0.10	*D/CD*=0.15	*D/CD*=0.20	*D/CD*=0.25	*D/CD*=0.30
0.02	0.03	0.045	0.07	0.1

Theoretical calculation verification of OCCA.

To investigate the influence mechanism of OCCA on the convergence morphology of the annular jet, this study quantitatively calculates the radial collapse velocities of the inner and outer liner elements based on the liner collapse theory. The annular liner is uniformly divided into 20 elements from the apex toward the inner and outer liner bases along the generatrix (numbered 1 to 20, with element 1 near the apex and element 20 near the base). The following radial velocity variables are defined: V_n is the radial velocity of the inner liner element; V_w is the radial velocity of the outer liner element (uncompensated state); and $V_w(E_w)$ is the radial velocity of the outer liner element after applying outer charge compensation.

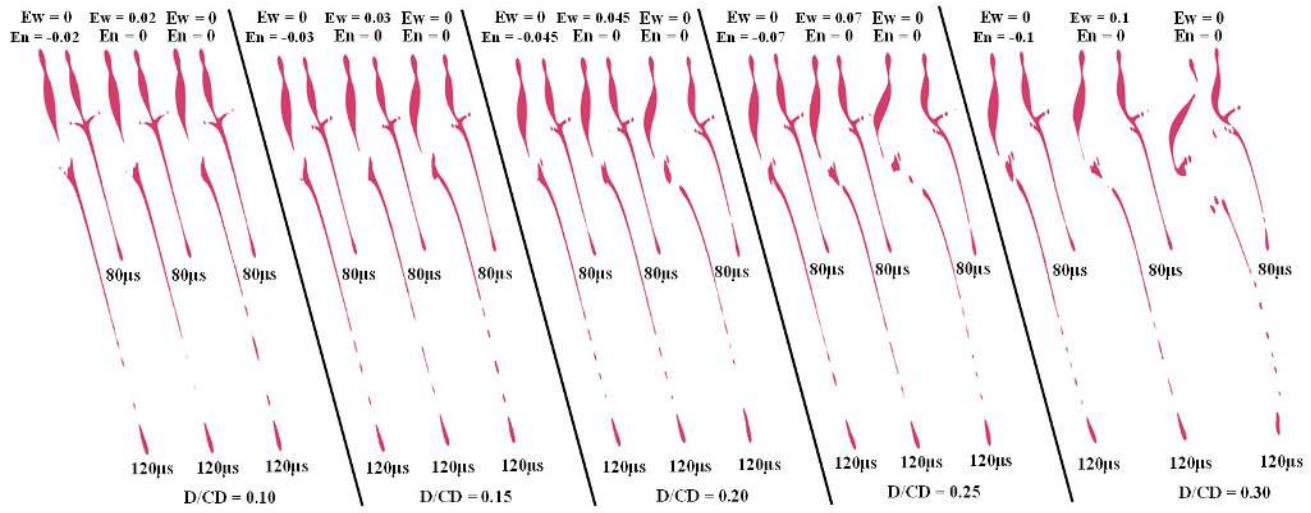

Figure 8. Morphological disparities in the formation of HASC with varying D/CD ratios at 80 μs and 120 μs, with and without OCCA

The definition of OCCA, as described in Section 3.3.1, is jointly determined by E_w and E_n,(OCCA = $E_w - E_n$). To simplify the theoretical analysis, this section temporarily assumes the inner compensation amount E_n = 0, meaning OCCA is adjusted solely by varying the outer charge compensation amount E_w. This simplification establishes a linear proportional relationship between OCCA and E_w (OCCA = E_w), allowing for an intuitive observation of the effect of changes in the outer compensation on the velocity field.

Figure 9 presents the radial velocity distribution at different liner element positions. The following patterns can be observed from the figure:

(1) Distribution trend of radial velocity along the liner generatrix: As the liner element moves from No. 1 (apex) to No. 20 (base), the corresponding radial charge thickness gradually decreases. Consequently, the absolute values of V_n and V_w exhibit a monotonic decreasing trend. This result aligns with classical collapse theory, validating the reliability of the computational model.

(2) Adjustment pattern of compensation amount with varying structural parameters: When the structural parameters of the HASC change (e.g., an increase in *D/CD*), the required outer charge compensation amount E_w increases accordingly. As *D/CD* increases, the difference in radial velocity before and after compensation, $\Delta V_w = |V_w(E_w) - V_w|$, progressively widens. This indicates that structures with larger *D/CD* require greater outer compensation to elevate the outer liner radial velocity to a level that matches the inner liner velocity, thereby restoring jet collimation.

The physical significance of the above pattern can be further understood in conjunction with the numerical simulation results shown in Figure 8: when the annular jet exhibits outward deflection and bulging, it implies a relative deficiency in the radial velocity of the outer liner. In this case, increasing V_w through the outer charge compensation amount E_w realigns the radial velocities of the inner and outer liners, allowing the jet morphology to return to a collimated state.

It should be noted that the theoretical model described above can only reveal the qualitative relationship between the structural parameter (*D/CD*) and the compensation amount (an increase in *D/CD* leads to a greater increase in outer liner velocity, which in turn results in a larger required outer charge compensation amount). However, it cannot directly provide the specific OCCA values for different structural parameters. This limitation arises because the theoretical formulation assumes an ideally uniform charge distribution and does not account for practical charge boundary effects; the radial velocity only characterizes the initial collapse stage, while subsequent jet stretching and breakup processes involve more complex hydrodynamic behaviors; and the coupling effects of multiple factors—such as the curvature of the annular liner, material strength, and detonation wave propagation—are difficult to fully capture with a simplified theoretical approach. Therefore, for HASC with varying structural parameters (*D/CD*, *L/D*, *b/D*, etc.), the precise OCCA values still need to be predicted using numerical simulations combined with machine learning methods, which constitutes the main focus of the subsequent study.

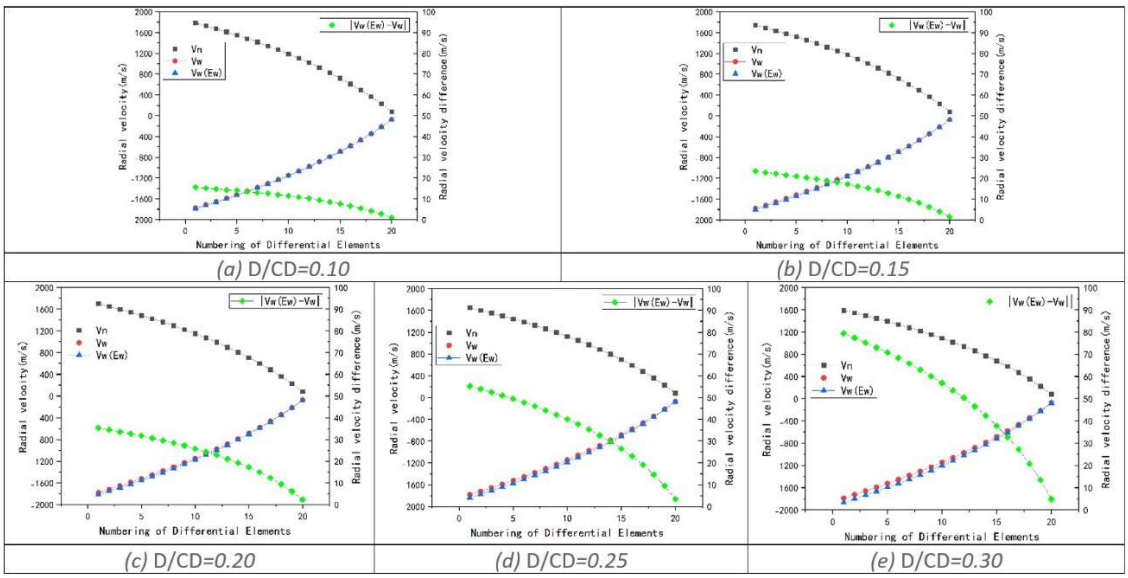

Figure 9. Theoretical verification results of OCCA for HASC under different D/CD ratios

Training and Performance Analysis of MLP

MLP Model

The formation morphology of annular jets presents a highly complex, nonlinear challenge, influenced by factors like liner caliber, charge height, and cone angle, whose interactions are hard to model mathematically. However, the MLP (Multi-Layer Perceptron) excels in nonlinear mapping and generalization, making it ideal for predicting the OCCA required for annular jet formation. Its multi-layer structure captures intricate interactions among HASC warhead parameters, while gradient descent-based backpropagation refines weights and biases during training, enhancing generalization for accurate OCCA prediction. Given HASC's complexity and nonlinearity, and MLP's strengths in such problems, it is chosen as the predictive model.

The MLP neural network comprises input, hidden (multi-layer), and output layers. It calculates outputs via forward propagation, backpropagates errors layer-by-layer, and adjusts weights/biases using gradient descent to approximate target values. The MLP framework for HASC-OCCA prediction in this study is shown in Figure 10.

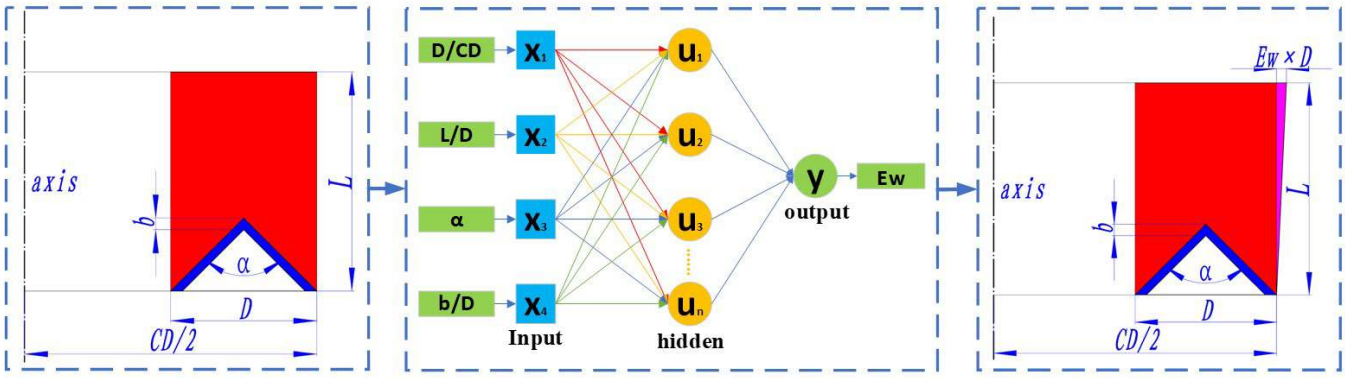

Figure 10. MLP Prediction Framework for HASC-OCCA

MLP parameters in vector form: input $X=(x_1,x_2,...,x_i,...,x_n)^T$, hidden output $Y=(y_1,y_2,...,y_j,...,y_m)^T$, input-to-hidden weights $W=(W_1,W_2,...,W_k,...,W_m)^T$ and bias $b=(b_1,b_2,...,b_k,...,b_m)^T$, output $O=(o_1,o_2,...,o_k,...,o_m)^T$, hidden-to-output weights $V=(V_1,V_2,...,V_j,...,V_m)^T$ and bias $r=(r_1,r_2,...,r_k,...,r_m)^T$.

For the hidden layer, activation functions are required to validate MLP accuracy: *f* (*x*) denotes the activation function from input to hidden layer, while *g* (*x*) represents that from hidden to output layer.

Thus, the output of the j-th neuron in the hidden layer can be calculated as follows.

$$y_j = f\left(\sum_{i=1}^{n}\left(w_{ij}\cdot x_i + b_j\right)\right) \tag{25}$$

The output of the k-th neuron in the output layer can be computed as follows.

$$z_k = g\left(\sum_{j=1}^{n}\left(v_{jk}\cdot y_j + r_k\right)\right) \tag{26}$$

Commonly used activation functions include the following:
ReLU activation function: It maps all negative inputs to 0 while leaving positive inputs unchanged.

$$h(x) = \max(0, x) \tag{27}$$

The Purelin function: Being linear, its output scales unboundedly with input magnitude.

$$h(x) = x \tag{28}$$

The Logistic Sigmoid: Maps inputs to (0,1) as probabilities, ideal for binary classification and bounded neural layers, introducing nonlinearity.

$$h(x) = \frac{1}{1+e^{-x}} \tag{29}$$

However, this merely represents a single-round prediction. If the predicted values significantly deviate from the true values, a learning algorithm is required to optimize weights and biases, employing the Mean Squared Error (MSE) as the loss function, where $y_{pred(i)}$ is the predicted value and $y_{ture(i)}$ is the true value.

$$L = \frac{1}{n}\sum_{i=1}^{n}\left(y_{pred(i)} - y_{ture(i)}\right)^2 \tag{30}$$

Gradient descent is then applied to iteratively refine weights and biases. The loss function L decreases iteratively until convergence, at which point the MLP output is finalized.

$$\begin{cases} w_{new} = w - \eta\dfrac{\partial L}{\partial w} \\ b_{new} = b - \eta\dfrac{\partial L}{\partial b} \end{cases} \tag{31}$$

Training of MLP

Theoretical calculations have identified four input parameters for the MLP model (as listed in Table 6). Through permutation-combination and curve-fitting, 1,431 data pairs were generated for MLP training and testing. Figure 11 illustrates the fitted curves of OCCA for various HASC structures, while Figure 12 presents a 4D visualization of the corresponding data. Notably, OCCA varies significantly across HASC structures, generally increasing with rising *D/CD*, *L/D*, and *α*, with their influence ranked as *α* > *D/CD* > *L/D*. Conversely, *b/D* exhibits negligible impact on OCCA.

Table 6. Parameter table for different HASC structures

D/CD	*L/D*	*b/D*	*α*
0.10 ~ 0.30	1.00 ~ 2.00	0.08	60°~120°
0.10 ~ 0.30	1.50	0.06 ~ 0.12	90°

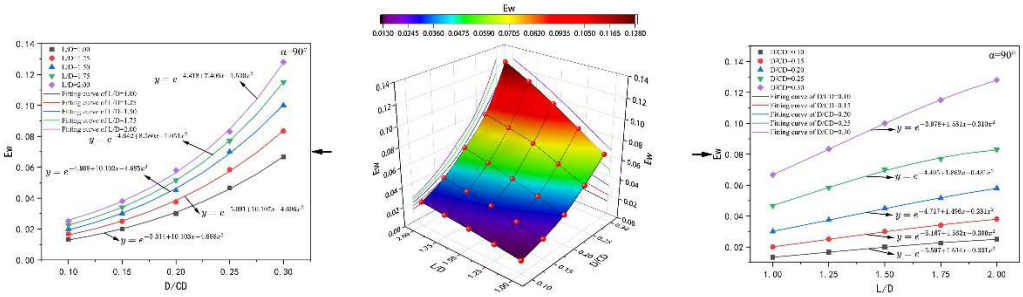

(a)Fitted OCCA curves for annular charges under α=90° and b/D=0.08, across varying D/CD and L/D ratios

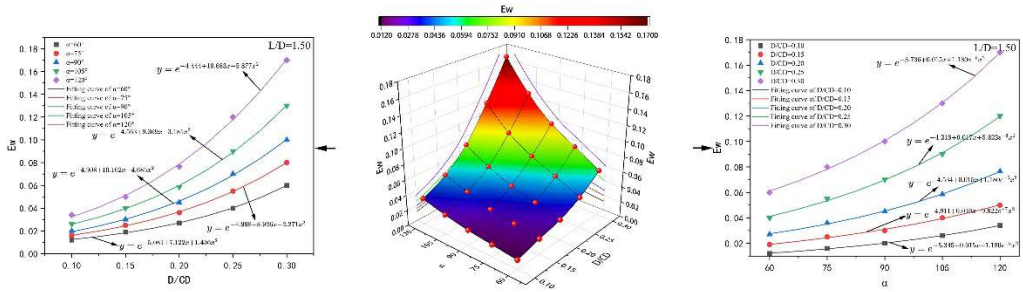

(b)Fitted OCCA curves for annular charges at L/D=1.50 and b/D=0.08, across varying D/CD and α angles

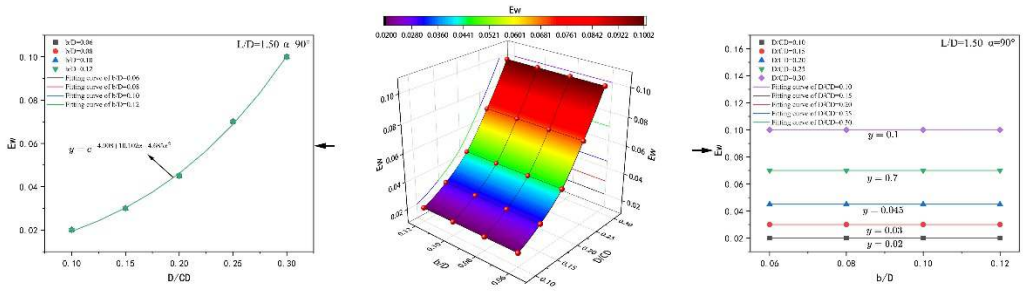

(c)Fitted OCCA curves for annular charges at L/D=1.50 and α=90°, across varying D/CD and b/D ratios

Figure 11. Fitted OCCA curves for partial HASC structures

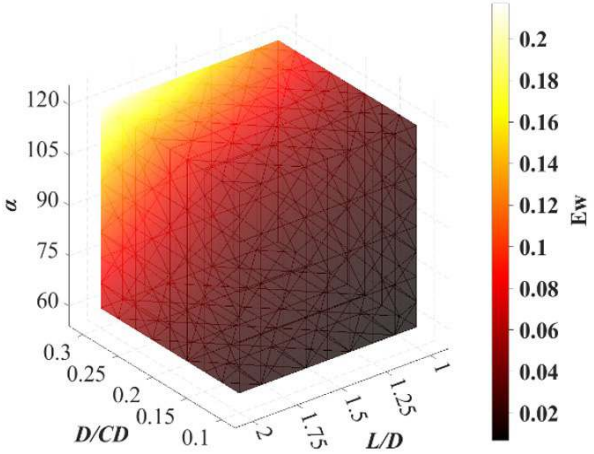

Figure 12. 4D visualization of HASC-OCCA

The MLP model constructed in this study takes input parameters that influence the formation morphology of annular jets, including the ratio of the liner cross sectional caliber to the charge diameter (*D/CD*) for HASC, the ratio of the charge height to the liner sectional diameter (*L/D*), the cone angle (α) of the annular liner, and the ratio of the liner apex thickness to the liner sectional diameter (*b/D*), with the output parameter being OCCA. The number of hidden layers, neuron count, and learning rate are critical parameters affecting MLP performance, which are determined through iterative optimization.

Performance Analysis of the MLP Model

In this study, the MLP model employs 1 hidden layer with 6 neurons, a learning rate of 0.001, convergence error of 1e-6, and max 50,000 iterations. Iteration stops upon reaching the iteration limit or convergence error, and MLP results are output.

Figure 13 illustrates the evolution of MSE for training, validation, and test datasets across iterations. The MLP model achieved convergence at the 53rd iteration, with a minimum MSE of 8.2926e-07. During these 53 iterations, MSE curves for all datasets declined sharply in the first 10 iterations before stabilizing, with no overfitting observed among training, validation, and test data, indicating robust MLP training performance.

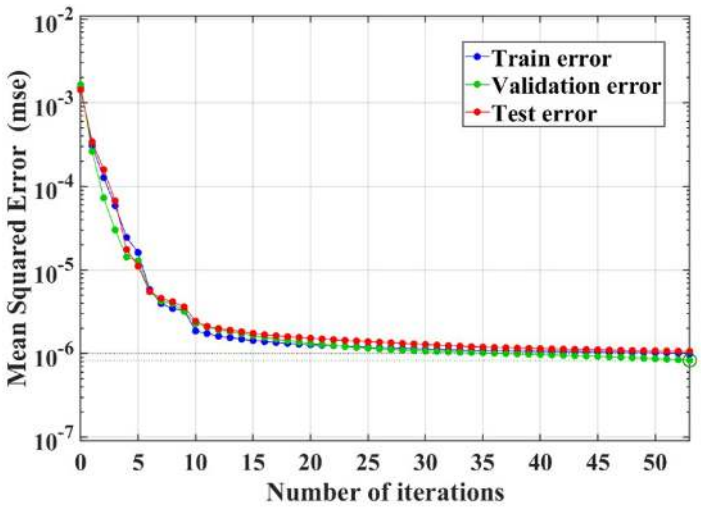

Figure 13. Variation of MSE with iteration

Figure 14 shows a comparison between predicted and actual values for the MLP test set. Among the 270 samples in the test set, the predicted values exhibit small deviation from the actual values on the scatter plot. The mean relative error of the test set, calculated using the following formula, is 0.013988. This demonstrates the MLP model's strong generalization capability within the data range.

$$error = \frac{1}{N}\sum_{i=1}^{N}\frac{\left|y_{pred(i)} - y_{true(i)}\right|}{y_{true(i)}} \tag{32}$$

In the formula, *error* is the mean relative error, *N* is the number of samples in the test set, $y_{pred(i)}$ is the predicted value, and $y_{ture(i)}$ is the actual value.

Cross-Validation and Multi-Model Performance Comparison of the MLP Model

To comprehensively evaluate the performance of the proposed Multilayer Perceptron (MLP) model in predicting the Optimal Charge Compensation Amount (OCCA), this section presents an analysis from two perspectives. First, the stability and generalization capability of the MLP model are examined through 5-fold cross-validation. Subsequently, the MLP model is compared horizontally with three commonly used machine learning models—Support Vector Regression (SVR), Random Forest, and Multiple Linear Regression—using boxplots and tabular data to quantitatively assess the prediction accuracy and robustness of each model.

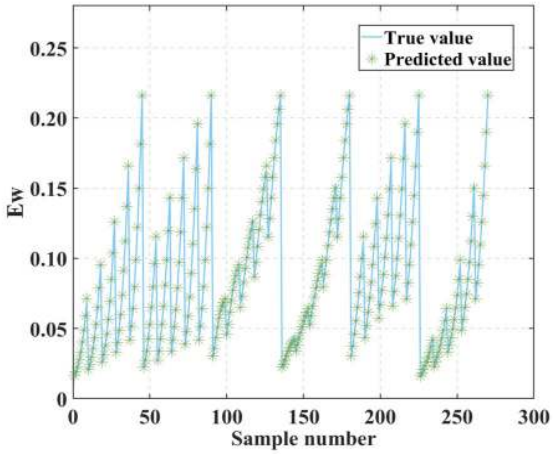

Figure 14. Comparison chart between predicted values and actual values

Stability Analysis of MLP Model via Cross-Validation

Figure 15 illustrates the Mean Absolute Percentage Error (MAPE) for each fold of the 5-fold cross-validation of the MLP model, along with its fluctuations. As observed in the figure, the MAPE values for the five folds are 1.55%, 1.53%, 1.52%, 1.65%, and 1.43%, respectively, ranging from 1.43% to 1.65%. The calculated average MAPE across the five folds is 1.54%, indicating that the MLP model exhibits highly consistent predictive performance across different training/testing data splits, with no signs of overfitting. This demonstrates excellent stability and generalization capability, validating the rationality of the model architecture and hyperparameter selection, and providing a reliable foundation for subsequent practical applications.

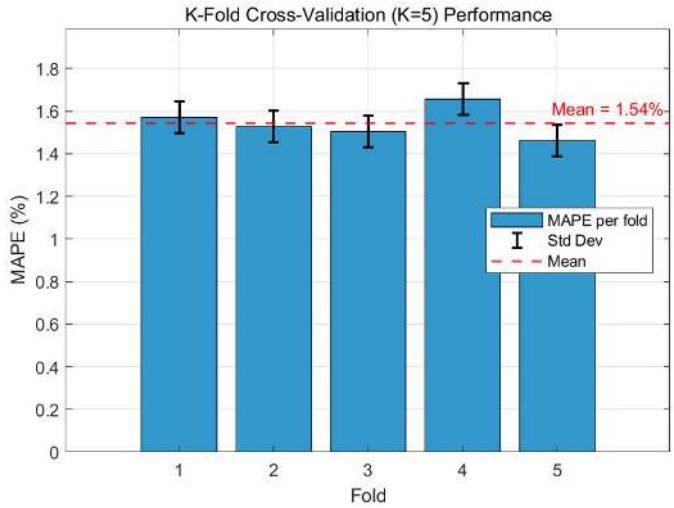

Figure 15. Fluctuation of MAPE for the MLP model in 5-fold cross-validation

Comparative Analysis of Multi-Model Performance

To further validate the superiority of the MLP model, it was compared with SVR, Random Forest, and Linear Regression under the same 5-fold cross-validation setting. Figure 16 presents boxplots that visually depict the distribution characteristics of the three metrics—RMSE, R^2, and MAPE—for each model, while Table 7 summarizes the detailed performance metrics (mean ± standard deviation).

From the boxplot distributions in Figure 16, the following features can be observed: the MLP model exhibits the smallest RMSE, with the narrowest box located at the lowest position, indicating the smallest and most stable prediction error. The RMSE values of SVR, Random Forest, and Linear Regression increase sequentially, accompanied by progressively wider boxes and greater dispersion. The median R^2 of the MLP model is close to 1.00, with the box nearly collapsed into a line, demonstrating that the model explains nearly all the variance in the target variable.

Although the R^2 values of the other models are also relatively high, their boxes are wider, indicating slightly lower stability. The MAPE of the MLP model is significantly lower than those of SVR, Random Forest, and Linear Regression. The narrowest box of the MLP model further confirms its robustness.

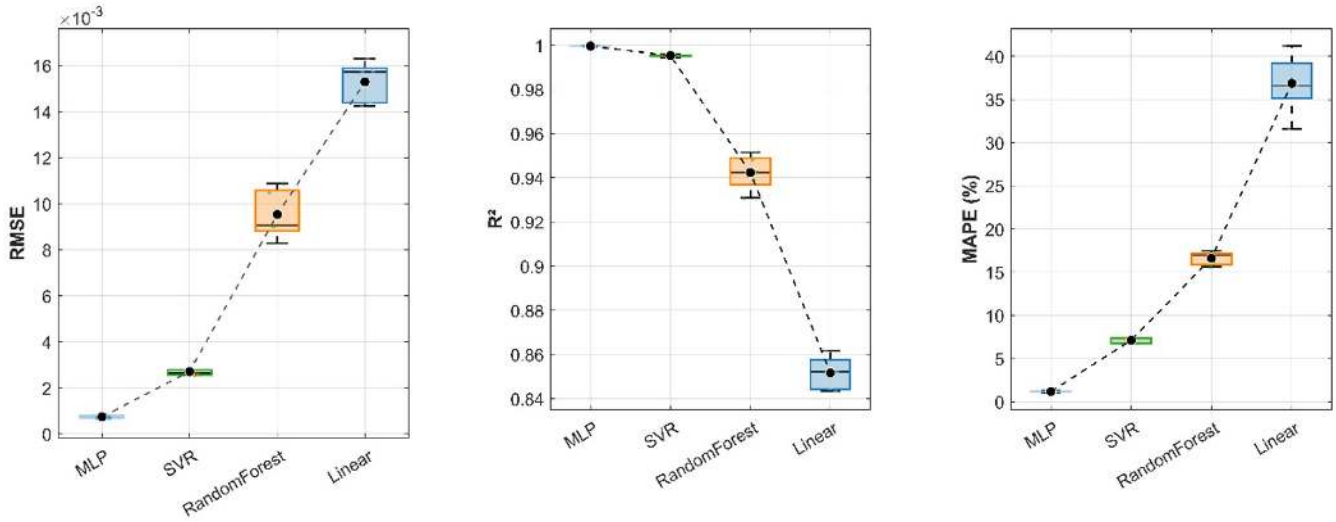

Figure 16. Boxplot comparison of the four models under 5-fold cross-validation

Table 7. Performance comparison of different models under 5-fold cross-validation (mean ± standard deviation)

Model	RMSE	R^2	MAPE (%)
MLP (this study)	0.001 ± 0.0002	0.999 ± 0.001	1.54 ± 0.07
SVR	0.0025 ± 0.0005	0.995 ± 0.002	7.13 ± 0.33
Random Forest	0.0095± 0.001	0.942 ± 0.008	16.62 ± 0.78
Linear Regression	0.0155 ± 0.001	0.852 ± 0.008	36.86 ± 3.51

As shown in Table 7, the MLP model achieves an R^2 of 0.999 ± 0.001, almost perfectly explaining the variance of the target variable, while the R^2 values of the other models are inferior, indicating that Random Forest and Linear Regression struggle to adequately capture the complex nonlinear relationship between OCCA and the input structural parameters. The MLP model exhibits the smallest standard deviation across all metrics, consistent with the observation that its box in Figure 16 is the narrowest. In contrast, SVR and Random Forest show relatively larger standard deviations and more pronounced performance fluctuations. Linear Regression has the poorest stability, with a MAPE standard deviation as high as 3.51%, confirming that a simple linear model cannot adequately describe the underlying relationship between the input structural parameters and OCCA. Among the three nonlinear models (MLP, SVR, and Random Forest), all demonstrate superior performance, with MLP achieving the best fitting results due to its deep architecture.

Formation of HASC under OCCA Predicted by MLP

MATLAB Program for Generating Random Parameters

Based on this study's logic, for HASC design: first, set liner cross sectional caliber *D*; then determine charge diameter *CD* and height L to get *D/CD* and *L/D*; next, define annular liner conical angle *α*; finally, specify liner apex thickness *b* for *b/D*. Input these parameters (*D/CD*, *L/D*, *α*, *b/D*) into the MLP model to obtain OCCA.

Table 8. Reasonable range structural parameters from MATLAB random program

D/mm	*CD*/mm	*L*/mm	*α*/°	*b*/mm
3.4	12	3.9	67	0.35
100	421	177	135	6.4
106	620	244	129	11.6
91	284	201	131	8.7

Table 9. OCCA predicted by MLP model for random HASC structures

D/CD	*L/D*	*α*	*b/D*	E_w
0.2833	1.1471	67	0.1029	0.0399
0.2375	1.77	135	0.064	0.1651
0.1710	2.3019	129	0.1094	0.1131
0.3204	2.2088	131	0.0956	0.3043

After generating four sets of random HASC parameters (*CD*, *D*, *L*, *α*, *b*) using MATLAB, the random program was adjusted to ensure the derived *D/CD*, *L/D*, *α*, and *b/D* values of these samples fell outside the data range, testing its generalization. If the predicted OCCA annular jet forms well without deviation, the MLP is deemed to have good generalization. Table 8 lists reasonable range structural parameters from MATLAB random program, while Table 9 shows OCCA results from MLP predictions.

Comparative analysis of annular jet formation morphology after MLP-predicted OCCA

The annular jet formation diagrams of random structures designed by MLP are shown in Figure 17 and Figure 18 (showing the upper part along the symmetry axis of the HASC cross-section). When the liner cross-sectional caliber *D* and charge diameter *CD* vary, the magnitudes of *L* and *b* correlate with *D*, ultimately resulting in different HASC structures. Therefore, according to the definition of geometric similarity in similarity theory, for different HASCs in Table 8, the required data is not the formation morphologies of different HASCs at the same time, but rather the formation morphologies at the same time after scaling (shrinking or enlarging) the HASC models in Table 8 proportionally to the same *D* value (*D* = 100 mm in this study).

The annular charge is initiated at 32 points. After scaling the original model according to similarity theory, at 80 μs, the annular jet has initially formed. Different HASC structures result in varying fracture times of the annular jet's head. By 160 μs, the annular jet continues to elongate.

Through numerical simulation, it is found that even for annular jets outside the data range, after MLP-predicted OCCA, they still exhibit favorable formation morphology without deviation. Under high stand-off conditions, the predicted OCCA annular jets can fly steadily along the axis of the liner cross-section, ensuring jet concentration and no deviation. According to relevant research by many scholars, such jets demonstrate superior penetration performance.

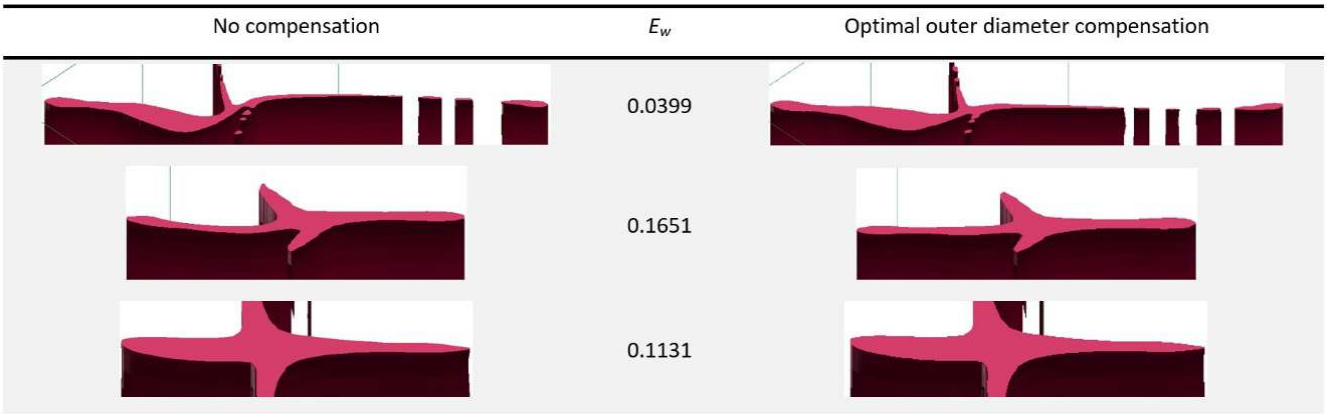

Figure 17. Morphological differences in the annular jet formation of the random HASC structure at 80μs

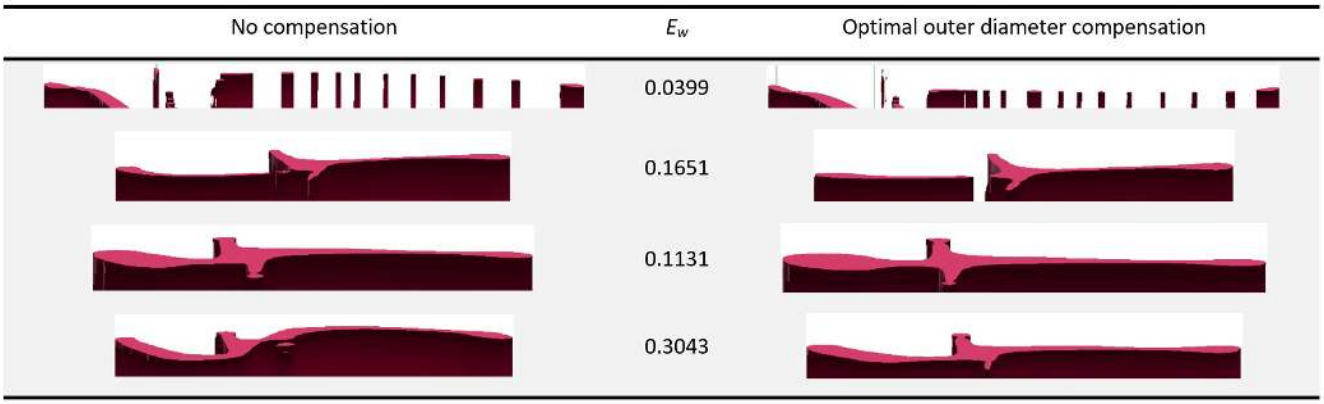

Figure 18. Morphological differences in the annular jet formation of the random HASC structure at 160μs

Equivalence and Validation

In Section 3.1, when validating the reliability of the numerical simulation, an eccentric-liner annular shaped charge structure was employed. On the surface, it appears that the optimization of annular jet deviation is achieved by adjusting the liner; however, in reality, the liner wall thickness remains unchanged, with minimal mass variation between the inner and outer rings of the annular liner. Thus, the optimization is essentially accomplished by adjusting the radial charge mass corresponding to the inner and outer rings.

To verify this judgment and further assess the reliability and broad applicability of the charge compensation method and the MLP model, the HASC structure of the eccentric shaped charge liner in Figure 6 is equated from the structure in Figure 19(a) to that in Figure 19(b). By shifting the liner apex from point B to point C, an eccentric shaped charge liner is formed. From the cross-section of the HASC, triangle ABC is equated to triangle EFG, where the heights of the two triangles are equal. Adjusting the lengths of the triangle bases (BC and FG) ensures that the volumes of the triangular annular charges obtained after a full rotation are equal, thereby achieving charge equivalence—that is, ensuring equal radial charge quantities for the micro-elements of the shaped charge liners in both structures. Similarly, triangle DBC is equated to triangle HIJ.

A 32-point initiation is employed to observe the fully formed configuration of the annular jet. According to Figure 19(d) and Figure 19(e), both exhibit similar formation morphologys without a casing. In contrast, as shown in Figure 19(g) and Figure 19(h), after adding a casing, their configurations revert to relatively straight and similar shapes (albeit with slight inward deviation). Thus, it is evident that the casing also significantly optimizes the deviation of HASC, which corresponds to the results of dimensional analysis.

An MLP model was used to predict the OCCA of the HASC structure for the non-eccentric liner in Figure 5, with numerical simulations as shown in Figure 19(c). Since this study focuses on optimizing annular jet deviation via charge compensation amount, Figure 19(f) shows the casing-free jet already has a good formation morphology. Adding a casing affects its axial and radial velocities, while casing thickness variations have minor impact (Kelly R J. 1994). Thus, when adding a casing, adjusting its inner and outer thicknesses while keeping materials constant is needed to maintain a undeviated jet configuration, as in Figure 19(i). Figure 19(f) and Figure 19(i) reveal that casing addition alters the jet's velocity gradient, shifting the HASC jet-slug boundary forward and reducing jet content while increasing slug content in the annular penetrator.

From Figure 19(g) and Figure 19(i), the annular jet with 12-point initiation shows poor forming, while both the eccentric liner- and charge compensation-optimized HASCs fully penetrate the target. To further compare penetration performance, the stand-off distance was increased from 1.12D to 4D to test penetration capability and collimation under large stand-off conditions. As shown in Figure 19(j) and Figure 19(k), the charge compensation-optimized HASC achieves larger penetration diameter and depth, confirming better collimation during large stand-off flight. The smaller diameter of the eccentric liner-optimized HASC is due to slight inward deviation of the annular jet.

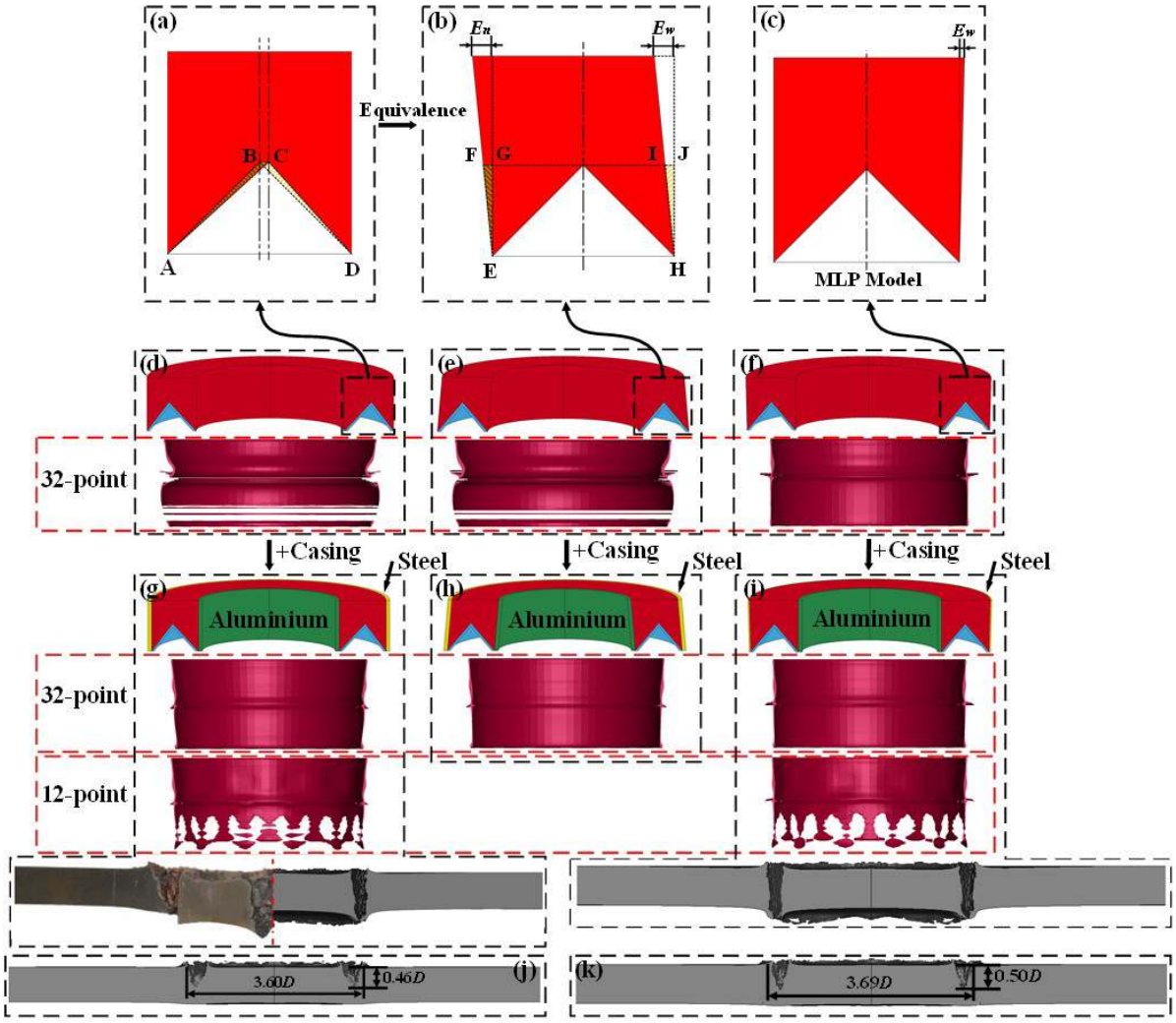

Figure 19. Overall diagram for equivalence and validation

Results and discussion

This study proposes a HASC-OCCA prediction model integrating finite element method with multilayer perceptron (FEM-MLP) based on a novel charge compensation method. First, dimensional analysis and theoretical calculations identify all factors influencing the morphological stability of annular jets, enabling the selection of four input parameters for the MLP model. Experimental validation confirms the reliability of the numerical simulations, which generate 1,431 data points for MLP training and testing. The trained MLP is then used to predict the OCCA of random HASC structures, and the charge compensation method is applied to equivalent HASC structures, demonstrating its broad applicability. Finally, numerical simulations validate the MLP's generalization capability and optimize experimental structures from the reference to achieve superior forming and penetration performance. The following key conclusions are drawn:

(1) The deviation of HASC is jointly influenced by the liner, charge, and casing. Optimization of HASC formation cannot be separated from the scope of these three elements. When studying any single aspect, variations in the other two aspects should be taken into account, which has been validated through the comparison between the numerical simulation and experimental target plate results in this study.

(2) *D/CD* is the variable that needs to be established first in the study of HASC. Optimization research on HASC should commence only after the value of this variable is clearly defined, and optimization studies for HASCs with different *D/CD* values cannot be directly applied to one another.

(3) On a general basis, HASC-OCCA exhibits an upward trend with the increase of *D/CD*, *L/D*, and α. The influence of these three factors on OCCA intensifies successively in the order of *L/D*, *D/CD*, and α, while the magnitude of *b/D* has a negligible impact on HASC-OCCA.

(4) The MLP prediction model for HASC-OCCA demonstrates stable convergence during both training and testing phases. It achieves the convergence error at the 53rd iteration, with the minimum MSE of the MLP model reaching 8.2926e-07. Over these 53 iterations, no overfitting is observed among the training, validation, and test set data. Through 5-fold cross-validation, overfitting of the MLP model was avoided, ensuring its generalization capability. Compared with other predictive models, the MLP model achieved an RMSE of 0.001 and a MAPE of 1.54%, significantly lower than those of the comparison models. This validates that the MLP model constructed in this study can accurately and stably map the intrinsic relationship between the input structural parameters and OCCA.

(5) Through numerical simulation and MLP-based OCCA prediction, even for random samples outside the data range, the formed annular jet still exhibits a properly shaped configuration without deviation, flying steadily along the axial direction of the liner cross-section. This provides valuable design references for annular jet penetration of target plates, demonstrating the MLP model's excellent generalization capability.

(6) The charge compensation method exhibits broad applicability and can be used for equivalent validation of similar HASC structures. The HASC optimized by the charge compensation method does not deflect under high stand-off explosion conditions, demonstrating favorable formation morphology and collimation. Compared with the HASC optimized with a deflected liner, it achieves a larger penetration aperture and depth, offering design references for the penetration of target plates by annular jets under high stand-off explosion scenarios.

Acknowledgments

The authors would like to acknowledge receipt of the following financial support for the research, authorship, and/or publication of this article: This work was supported by the National Natural Science Foundation of China (Grant No. 12372360).

Author Contributions: Liudong Zheng: Methodology, Software, Validation, Formal analysis, Investigation, Data Curation, Writing - Original Draft, Visualization. Xin Jia: Resources, Writing - Review & Editing, Supervision, Project administration, Funding acquisition. Zhengxiang Huang: Conceptualization, Supervision, Project administration, Funding acquisition, Conceptualization. Yuze Chen: Conceptualization, Methodology, Software.

Data Availability: Research data is only available upon request.

Editor: Pablo Andrés Muñoz Rojas

References

Hu F, Wu H, Fang Q, et al. Impact performance of explosively formed projectile (EFP) into concrete targets[J]. International Journal of Impact Engineering, 2017, 109: 150-166.

Liu J, Long Y, Ji C, et al. Influence of layer number and air gap on the ballistic performance of multi-layered targets subjected to high velocity impact by copper EFP[J]. International Journal of Impact Engineering, 2018, 112: 52-65.

Wu J, Liu J, Du Y. Experimental and numerical study on the flight and penetration properties of explosively-formed projectile[J]. International journal of impact engineering, 2007, 34(7): 1147-1162.

Jia X, Huang Z, Zu X, et al. Experimental study on the performance of woven fabric rubber composite armor subjected to shaped charge jet impact[J]. International Journal of Impact Engineering, 2013, 57: 134-144.

Xu W, Wang C, Chen D. The jet formation and penetration capability of hypervelocity shaped charges[J]. International Journal of Impact Engineering, 2019, 132: 103337.

Xiao Q Q, Huang Z X, Jia X, et al. Shaped charge penetrator into soil–concrete double-layered target[J]. International Journal of Impact Engineering, 2017, 109: 302-310.

Lee W H. Oil well perforator design using 2D Eulerian code[J]. International Journal of Impact Engineering, 2002, 27(5): 535-559.

Elshenawy T, Li Q M. Influences of target strength and confinement on the penetration depth of an oil well perforator[J]. International Journal of Impact Engineering, 2013, 54: 130-137.

Niu Y, Huang Z, Jia X, et al. Research on the penetration performance of shaped charge jet into block stone concrete targets[J]. International Journal of Impact Engineering, 2024, 193: 105060.

Zhu Q, Huang Z, Xiao Q, et al. Theoretical and experimental study of shaped charge jet penetration into high and ultra-high strength concrete targets[J]. International Journal of Impact Engineering, 2018, 122: 431-438.

Jia X, Huang Z X, Zu X D, et al. Theoretical and experimental study on the effects of impact angle on the performance of kevlar woven fabric rubber composite armor against shaped charge jet impact[J]. Propellants, Explosives, Pyrotechnics, 2015, 40(6): 945-953.

Micković D, Jaramaz S, Elek P, et al. A model for explosive reactive armor interaction with shaped charge jet[J]. Propellants, Explosives, Pyrotechnics, 2016, 41(1): 53-61.

Zhang Z, Wang L, Ming F, et al. Application of Smoothed Particle Hydrodynamics in analysis of shaped-charge jet penetration caused by underwater explosion[J]. Ocean Engineering, 2017, 145: 177-187.

Cao C, Wang J, Kong L, et al. Study on the formation characteristics of underwater hemispherical shaped charge jet and its penetration performance into concrete[J]. Defence Technology, 2025, 47: 180-196.

Leidel D J. A design study of an annular-jet charge for explosive cutting[M]. Drexel University, 1978.

Wang C, Huang F, Ning J. Jet formation and penetration mechanism of W typed shaped charge[J]. Acta Mechanica Sinica, 2009, 25(1): 107-120.

Xu W, Wang C, Chen D. Formation of a bore-center annular shaped charge and its penetration into steel targets[J]. International Journal of Impact Engineering, 2019, 127: 122-134.

Xu W, Wang C, Yuan J, et al. Bore-center annular shaped charges with different liner materials penetrating into steel targets[J]. Defence Technology, 2019, 15(5): 796-801.

Zhang Z, Wang C, Xu W, et al. Application of a new type of annular shaped charge in penetration into underwater double-hull structure[J]. International Journal of Impact Engineering, 2022, 159: 104057.

Liu J, Du Z H. The effect of different multi-point initiation on the formation and penetration of annular EFP[J]. Applied Mechanics and Materials, 2013, 246: 718-722.

Jie L, Qing H, Jiandong G, et al. Experimental Study of Penetration Capability of an Annular-Shaped Charge under Multipoint Synchronous Initiation[J]. Shock and Vibration, 2023, 2023(1): 3334033.

LI Zhaoting, WANG Shuyou, SUN Shengjie, JIANG Jianwei, MEN Jianbing. Analysis of influencing factors on formation and penetration capabilitiesof asymmetric hollow annular shaped charge[J]. Explosion And Shock Waves, 2025, 45(1): 012301. doi: 10.11883/bzycj-2024-0074.

Hu Z, Wang Z, Yin J, et al. Formation and Penetration Capability of an Annular-Shaped Charge[J]. Mathematical Problems in Engineering, 2021, 2021(1): 6660189.

REN Siyuan, ZHANG Qingming, ZHANG Xiaowei, TIAN Zhimin. On the Perforation Characteristics of Concrete Wall Induced by Annular Jet and Central EFP Combined Warhead[J]. Acta Armamentarii, 2021, 42(8): 1569-1579. http://www.co-journal.com/CN/10.3969/j.issn.1000-1093.2021.08.001

Huang QT. Research on the formation mechanism of annular EFP. Nanjing University of Science and Technology, 2008. Chinese.

Hou J. Research on the formation and penetration of annular shaped-charge damage elements. Nanjing University of Science and Technology, 2023. Chinese.

Chen H. Research on the formation technology of hollow annular shaped-charge jets. Nanjing University of Science and Technology, 2023. Chinese.

Gao J. Research on the deflection mechanism of annular EFP. North University of China, 2024. Chinese.

Ponnarengan H, Rajendran S, Khalkar V, Devarajan G, Kamaraj L. Data-Driven Healthcare: The Role of Computational Methods in Medical Innovation. Comput Model Eng Sci. 2025;142(1):1–48. https://doi.org/10.32604/cmes.2024.056605

Rahman SIU, Abbas N, Ali S, Salman M, Alkhayat A, Khan J, et al. Deep Learning and Artificial Intelligence-Driven Advanced Methods for Acute Lymphoblastic Leukemia Identification and Classification: A Systematic Review. Comput Model Eng Sci. 2025;142(2):1199–1231. https://doi.org/10.32604/cmes.2025.057462

Koide R M, Ferreira A P C S, Luersen M A. Laminated composites buckling analysis using lamination parameters, neural networks and support vector regression[J]. Latin American Journal of Solids and Structures, 2015, 12(2): 271-294.

Mahmoodi M, Naderi A. Applicability of artificial neural network and nonlinear regression to predict mechanical properties of equal channel angular rolled Al5083 sheets[J]. Latin American Journal of Solids and Structures, 2016, 13(8): 1515-1525.

Cao C, Xia J, Tang K, et al. The formation and penetration characteristics of underwater shaped charge jets at varying depths: experiment, simulation, and machine learning[J]. Ocean Engineering, 2025, 339: 122164.

Wu B, Xu S, Meng G, et al. Research on structural parameter optimization of elliptical bipolar linear shaped charge based on machine learning[J]. Heliyon, 2022, 8(10).

Zhao Z, Li T, Sheng D, et al. Machine learning optimization strategy of shaped charge liner structure based on jet penetration efficiency[J]. Defence Technology, 2024, 39: 23-41.

CHEN Hao, ZU Xudong, HUANG Zhengxiang. Optimization of Annular Liner Based on BP Neural Network and Genetic Algorithm. Journal Of Ballistics. 2022, 34(04): 1-7 https://doi.org/10.12115/j.issn.1004-499X(2022)04-001.

Xu W, Wang C, Yuan J. Impact performance of an annular shaped charge designed by convolutional neural networks[J]. Thin-Walled Structures, 2021, 160: 107241.

Chanteret P Y. An analytical model for metal acceleration by grazing detonation[C]//Proceedings of the 7th International Symposium on Ballistics. 1983: 515-524.

Kelly R J, Curtis J P, Bremer M. On analytic modeling of casing and liner thickness variations in a shaped charge[J]. Journal of applied physics, 1994, 75(1): 96-103.